*Laser & Photonics Reviews*

LASER & PHOTONICS REVIEWS

www.lpr-journal.org

RESEARCH ARTICLE

# Conformal Aberration-Correcting Spaceplates

Yixuan Shao[1] | Zichan Wang[2] | Tianxiang Dai[1] | Robert Lupoiu[1] | Youngsik Kim[2] | Tom D. Milster[2] | Jonathan A. Fan[1]

[1]Department of Electrical Engineering, Stanford University, Stanford, USA | [2]James C. Wyant College of Optical Sciences, The University of Arizona, Tucson, USA

**Correspondence:** Jonathan A. Fan (jonfan@stanford.edu)

**Received:** 9 September 2025 | **Revised:** 5 December 2025

**Keywords:** aberration | flat optics | imaging system | nanophotonics | spaceplates | thin-film optics

## ABSTRACT

We present conformal aberration-correcting spaceplates (CAS), curvilinear freeform spaceplates on refractive surfaces that support tailored space expansion and compression as a function of incident angle. We investigate CAS on spherical surfaces and show that these systems can support variations in optical power and enable aberration correction in conceptually new ways: they possess spherical symmetry around the optical stop that naturally corrects for field-dependent aberrations, and they simultaneously function as aspheres with an axis of symmetry aligned with the field angle, thereby correcting for spherical aberration. CAS can be accurately designed and simulated using an angle-dependent effective index description together with full-wave analysis, and we comprehensively model CAS on convex spherical surfaces. These concepts point to new opportunities enabled by hybrid nanophotonic-refractive systems that combine the complementary properties of nano-optics and bulk refractive optics to facilitate advanced optical functionality.

## 1 | Introduction

Optical systems engineering is predicated on the design of physical systems that perform tailored mappings of incident rays to outgoing rays in a field-dependent manner. Conventionally, these systems perform optical transformations using ray interactions with dielectric interfaces, together with ray propagation within components (Figure 1A). The interactions between rays and interfaces are defined by Snell's law and are local: the optical response depends only on the point of interaction, the phase response is independent of the incident ray wavevector, and there is no lateral displacement between the incident and transmitted rays at the interface. While local interactions at interfaces are the predominant basis for designing optical systems today, they limit the ability of optical elements to precisely manipulate individual rays, particularly under wide field-of-view (FOV) and large aperture conditions, ultimately necessitating the use of complex multi-element assemblies [1].

Concepts that introduce new types of light-matter interactions at interfaces can offer new degrees of freedom in the optical design landscape that can further enhance optical system performance. In the context of local interfacial responses, structured nanophotonic devices in the form of diffractive and metasurface optics can yield local designer phase responses that are described using a generalized version of Snell's law [2–15]. Beyond local responses, devices featuring non-local light-matter interactions, which are the focus of this study, can exhibit qualitatively different behavior involving tailored interactions between interfaces and rays as a function of incidence angle and wavelength [16–21]. More specifically, non-local interfacial interactions are characterized by phase responses that are dependent on the incident ray wavevector, and these angle-dependent phase responses are equivalently framed as lateral displacements between the incident and transmitted rays [22].

Non-local interfacial interactions are realized in various photonic systems. They arise naturally at dielectric interfaces under con-

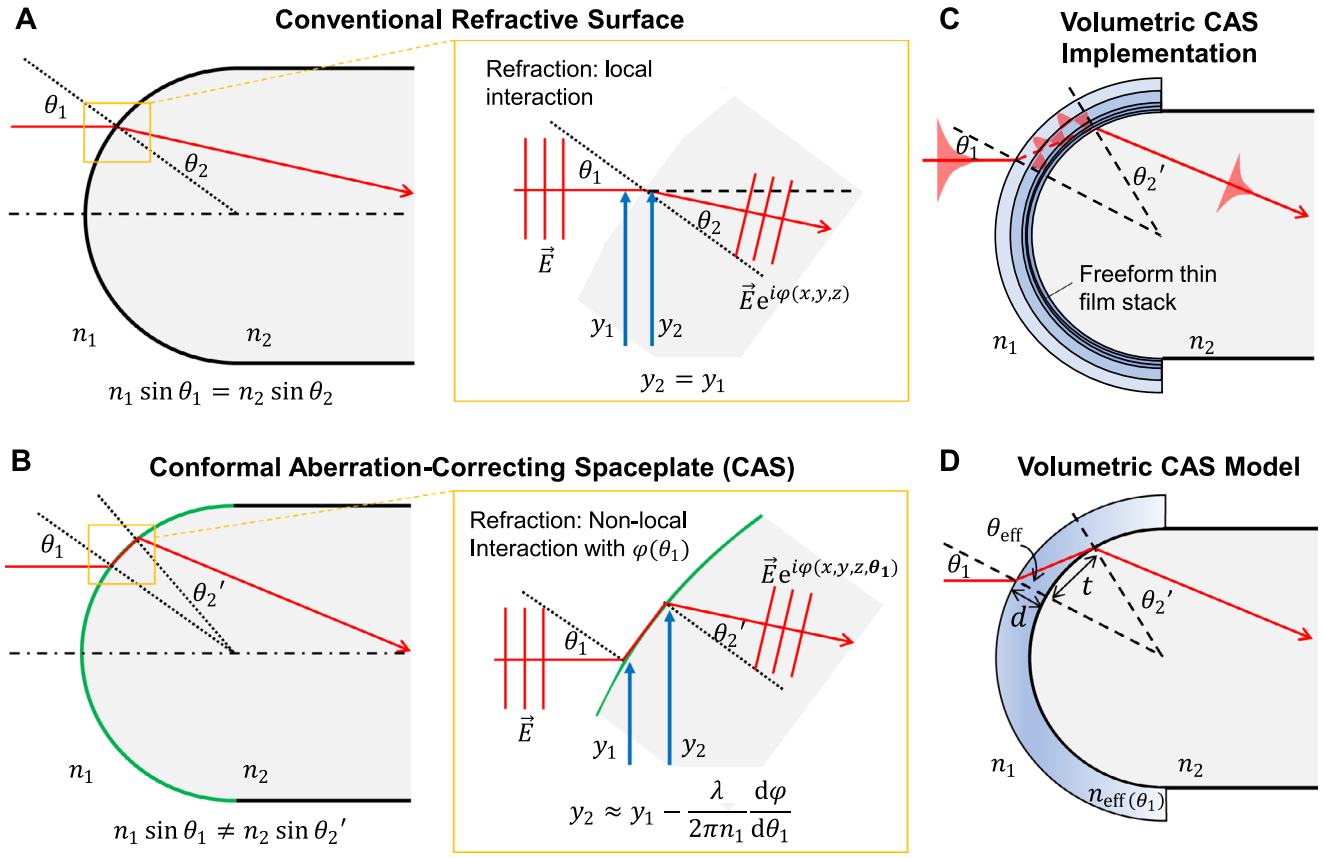


**FIGURE 1** | Conformal aberration-correcting spaceplate (CAS) concept. (A) Conventional ray propagation in a curved dielectric system. Rays at interfaces undergo refraction, which is defined by Snell's law. These optical interactions are local, and the incident and transmitted rays at the interface have the same position. (B) Ray propagation in a hybrid CAS-refractive system for an idealized ultrathin CAS interface. CAS conceptually functions as a generalized spaceplate that can expand or compress space as a function of incidence angle. As such, rays incident on the CAS experience a relative lateral shift of the transmitted ray as well as a modified tilt angle $\theta_2'$. These optical interactions are non-local and can be captured with a CAS phase response $\varphi$ that is a function of incidence angle $\theta_1$. (C) Physical CAS implementation. CAS can be realized using a volumetric thin-film stack, which utilizes engineered thin-film interference to achieve a desired transfer function response. (D) Simplified CAS model. The CAS is represented as a volumetric homogeneous medium with an angular-dependent effective index. Refraction at the air-CAS and CAS-glass interfaces is described using Snell's law.

ditions of total internal reflection, where the phase responses are angle-dependent and lead to Goos-Hänchen shifts [23]. They can also be tailored in nanophotonic media such as photonic crystals, bound-states-in-the-continuum metasurfaces, multilayer metasurfaces, and multilayer thin film stacks [24–32]. Thin film stacks are a particularly versatile platform for non-local response engineering, as they are volumetric and can be designed to support tailored phase responses as a function of incidence angle [33, 34]. As an example, freeform thin film stack systems termed spaceplates were recently proposed and designed to exhibit transfer functions matching that of free space, serving as a physical optic capable of effectively mimicking propagation through space [35–43]. While significant work has been done in understanding the underlying physics and design principles behind non-local photonic devices generally and spaceplates specifically, it remains an open question how these devices can integrate with refractive optics to improve optical system performance.

We present conformal aberration-correcting spaceplates (CAS), which are curvilinear freeform spaceplates that conform to and are co-designed with refractive surfaces. These hybrid nano-refractive optical systems combine non-local interfacial ray interactions with ray propagation in new ways, presenting an alternative pathway to aberration correction in a compact system form factor. We note that flat spaceplates combined with refractives have been previously investigated in the context of aberration correction [22], but CAS-based systems are qualitatively different as they have a symmetry defined by the refractive surface, which is critical when managing on- and off-axis aberrations. Specifically, the spherical symmetry of CAS prevents the introduction of field-dependent aberrations that would otherwise arise from integrating a planar spaceplate onto a curved lens. Furthermore, we introduce for the first time an angular-dependent effective index model, which provides a framework to co-design CAS with refractive optical elements. The general operating principle is presented in Figure 1B and shows a single ray incident on the CAS, which is represented as the thin green interfacial layer on the refractive surface. The CAS is a spaceplate but with more general functionality: it can support a designed transfer function that enables the effective expansion or compression of space as a function of incidence angle, $\theta_1$. The transfer function can be framed in terms of a wavevector-dependent phase response, $\varphi(k_\parallel)$, where $k_\parallel$ is the wave vector component parallel to the CAS interface.

Interaction of the incident ray with the CAS leads to a laterally shifted transmitted ray. The total displacement is $-\partial\varphi/\partial k_{\parallel}$ [44, 45], and the corresponding ray displacement on the spherical surface along the tangential direction is calculated $-(\lambda/2\pi n_1 \cos\theta_1)(\partial\varphi/\partial\theta_1)$. The displaced transmitted ray also experiences a modified tilt angle, $\theta_2'$, compared to that from a simple refractive process ($\theta_2$ in Figure 1A), due to the shifting of the ray on the curved interface and corresponding change of the surface normal direction. The combined displacement and tilt of the transmitted ray yields a modification of the ray trajectory to the focal plane. Importantly, due to the curved and convex geometry of the CAS, incident parallel rays located at different heights in the aperture interact with the CAS at different incidence angles. This registration of ray height with incidence angle, together with the freeform design of the angular-dependent CAS transfer function, enables the lateral shifts of rays within the aperture to be customized as a function of height in a manner that explicitly corrects for aberrations.

We emphasize that when we discuss the shifting of waves within a CAS, we are treating the wavefront as a superposition of local, finite-width beams. From a geometrical optics perspective, this can be viewed as a collection of rays. Each ray, which can be modeled locally as a finite beam, is then shifted by an amount corresponding to its incident wavevector. Fundamentally, an ideal plane wave has no defined spatial position and thus cannot, by definition, be "shifted". The shift must be a displacement of a finite-width beam's overall amplitude profile, which emerges from the constructive and destructive interference of the constituent plane wave components, each acquiring its respective phase from the non-local system.

The ultra-thin CAS depiction in Figure 1B provides a conceptual picture of how a CAS surface functions, but it is non-physical. Photonic devices supporting tailored optical responses as a function of incidence angle are ultimately required to be volumetric, which is specified by the theory of overlapping non-locality [46] and which generally sets minimum thickness bounds to non-local photonic media. To construct a physical CAS model, we consider volumetric spaceplates based on thin film dielectric stacks (Figure 1C). Thin film systems are ideal for CAS because their manufacturing is compatible with state-of-the-art lens coating techniques [36, 43, 47]. In addition, the simulation and freeform design of thin film stacks using the transfer matrix method (TMM) [48] is well understood, and the optimization landscape of thin film systems is large and capable of accommodating the types of optical responses we seek. While CAS are curvilinear, we justify our use of TMM to accurately model CAS when its thickness is small compared to the surface radius of curvature, and we treat the thin film stacks as locally planar in this limit. A more thorough examination of this approximation is provided later in this study.

To facilitate a design pipeline that connects our TMM-based CAS description with our desired systems-level shifting of transmitted rays across the device aperture, we propose a simplified CAS model in which the volumetric CAS is described by a homogeneous effective refractive index that is a function of incidence angle, $n_{\text{eff}}(\theta_1)$ (Figure 1D). To determine the effective index value for a given incidence angle $\theta_1$, CAS thickness $t$, and desired lateral ray displacement $d$, the effective refraction angle at the front CAS surface can be approximated as $\theta_{\text{eff}} = -\arctan(t/d)$ and the effective index can be subsequently evaluated using Snell's law: $n_{\text{eff}}(\theta_1) = n_1 \sin\theta_1 / \sin\theta_{\text{eff}}$. Our workflow for CAS design is as follows. First, we optimize $n_{\text{eff}}(\theta_1)$ of the CAS using geometric ray tracing. Second, we use $n_{\text{eff}}(\theta_1)$ to analytically solve for $\varphi(\theta_1)$, using the fact that tangential ray displacement follows $-\partial\varphi/\partial k_{\parallel}$. Third, we use freeform full-wave optimization methods based on TMM [22] to design the physical thin-film stack structure featuring the desired transfer function.

## 2 | Results and Discussion

### 2.1 | Design Principles

To investigate how CAS can perform aberration correction in optical systems, we focus on the design and utilization of CAS with individual spherical surfaces, which are fundamental building blocks of optical systems. We start with an analysis of air-to-glass convex surfaces, followed by an analysis of glass-to-air convex surfaces. The capabilities and limitations of spherical surfaces are understood by visualizing on- and off-axis parallel rays from air interacting with a spherical glass refractive surface (Figure 2A). The system contains an aperture stop at the surface center of curvature to maintain spherical symmetry. The advantages of spherical surfaces are clear: they are capable of focusing rays and intrinsically preserve the rotational symmetry of the system. However, for sufficiently wide apertures, spherical aberration is present for all fields. Positive spherical aberration manifests when the paraxial rays focus to a point that is further away than that focused by the marginal rays. We specify the paraxial focal plane for the on-axis field with the object at infinity as our reference plane when defining the focal plane offset.

A CAS applied to this spherical surface can correct for all aberrations except Petzval field curvature (Figure 2B). To understand how this works, we consider spherical aberration correction for the on-axis field incidence and observe that spherical aberration can be explicitly corrected by displacing the transmitted rays at the interface in customized ways. For example, the large downward lateral shift of the uppermost marginal ray has the effect of pushing the marginal ray focal plane further toward the paraxial focal plane, and opposite lateral shift adjustments for paraxial rays can be performed to move the focal plane closer. These lateral shifts equivalently correspond to an angularly dependent CAS effective index profile in which the marginal rays experience a relatively large CAS refractive index and rays of decreasing height experience lower CAS index values. When the rays are shifted appropriately, all rays focus to a single point, and the CAS-refractive system ultimately functions as an ideal asphere (Figure 2B).

Critically, the CAS-refractive system is spherically symmetric: the physical system comprises a spherical refractive surface with a thin film stack in which the films are spherical shells. As such, the on- and off-axis optical responses of the system are identical, and if spherical aberration is corrected for normal fields, it is also corrected for off-axis fields. In other words, for rays incident from an off-axis field, the aberration-corrected CAS-refractive system functions as an ideal asphere with an axis of symmetry aligned with the field angle (Figure 2C), and this condition holds

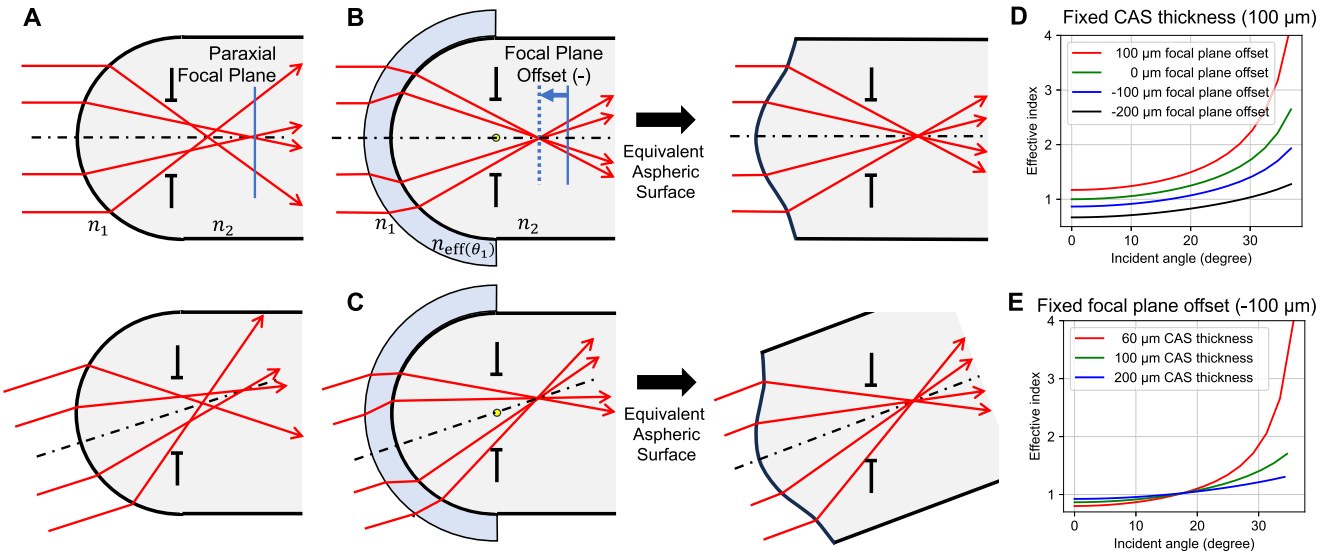


**FIGURE 2** | Aberration correction in a spherical air-to-glass CAS-refractive system. (A) Aberrations in a conventional spherical refractive system. The spherical symmetry eliminates all aberrations except spherical aberration and Petzval field curvature. (B,C) Aberrations in a CAS-refractive system. The CAS can explicitly correct for spherical aberration for (B) on-axis and (C) off-axis fields by judiciously tuning its $n_{\mathrm{eff}}(\theta_1)$ profile. The optical system behaves equivalently as an aspheric surface with an optical axis aligned with the field angle, for on- and off-axis fields. (D) CAS $n_{\mathrm{eff}}(\theta_1)$ required to achieve perfect imaging, for a fixed CAS thickness of 100 μm and focal plane offsets of 100, 0, –100, and –200 μm. The refractive radius of curvature is 1400 μm, and the wavelength is one micron. (E) CAS $n_{\mathrm{eff}}(\theta_1)$ required to achieve perfect imaging, for a fixed focal plane offset of –100 μm and CAS thicknesses of 60, 100, and 200 μm.

for all field angles. This ability for a single optical interface to support ideal aberration-free focusing is uniquely enabled by the wavevector engineering capabilities of our non-local photonic interface and cannot be realized using a flat or conformal local metasurface coupled with a spherical or aspherical surface.

To design aberration-correcting CAS for this single convex interface, we develop a differentiable ray tracing simulator compatible with our effective index CAS model, and we use gradient-based optimization to explicitly engineer an angular-dependent effective index profile that enables perfect focusing of parallel rays to a point. The radius of curvature of the refractive surface is set to 1400 μm, the wavelength is fixed to one micron, and the media to the left and right of the interface are air and fused silica, respectively. The aperture is set to produce an f-number of 2.55. The design task depends on the CAS thickness and focal plane offset, and we perform CAS optimization for a range of design parameters, which is summarized in Figure 2D,E. These plots show for all parameters that the ideal effective index is relatively large for large incidence angles and decreases for small angles, which matches our qualitative understanding of spherical aberration correction described above.

We first consider the case of fixed CAS thickness and different focal plane offsets (Figure 2D). CAS's ability to modify the focal-plane offset reflects its capacity not only to correct aberrations but also to adjust the optical system's power. For negative offset values, CAS adds power to the system, and effective index values less than one are required, which corresponds to the CAS performing space compression. For positive offset values, the CAS serves to reduce system power and expand space, leading to effective indices that are all greater than one. We see that while CAS can modify the optical power of the system, it does come with a cost: in the regime of large negative offset, space compression in spaceplates is known to be challenging to practically implement, and in the regime of large positive offset, implementation is limited by the refractive indices of the composing materials.

While the original spaceplate concept focused exclusively on the reduction of physical space, our CAS concept encompasses a more general interpretation of spaceplates that includes both the compression and expansion of physical space over the working angular range. The ability to expand space is important for two key reasons. First, for some aberration correction profiles, localized space expansion is required to perform effective correction. Second, compressive spaceplates are physically constrained by strict trade-offs between the compression ratio and the numerical aperture (NA) [49], and such constraints do not apply to space expanding devices. By prioritizing NA and aberration correction capabilities over the need for space compression, we can design devices that are more robust and capable for imaging systems.

We next consider the case of fixed focal plane offset and different CAS thicknesses (Figure 2E). Increasing the CAS thickness allows rays to propagate longer distances within the CAS layer, thereby generally requiring smaller effective index values to achieve a desired lateral ray shift compared to the case of thinner CAS systems. We observe that all effective index curves intersect at a single point, which corresponds to a specific incidence angle and an effective index equal to one. For rays incident at this angle, the CAS is effectively transparent, and the focal plane defined by these rays is due to refraction by the silica surface and specifies the focal plane of the whole system. We observe that this specific incidence angle partitions the effective index curves into two regimes, one with values less than one and the other with values

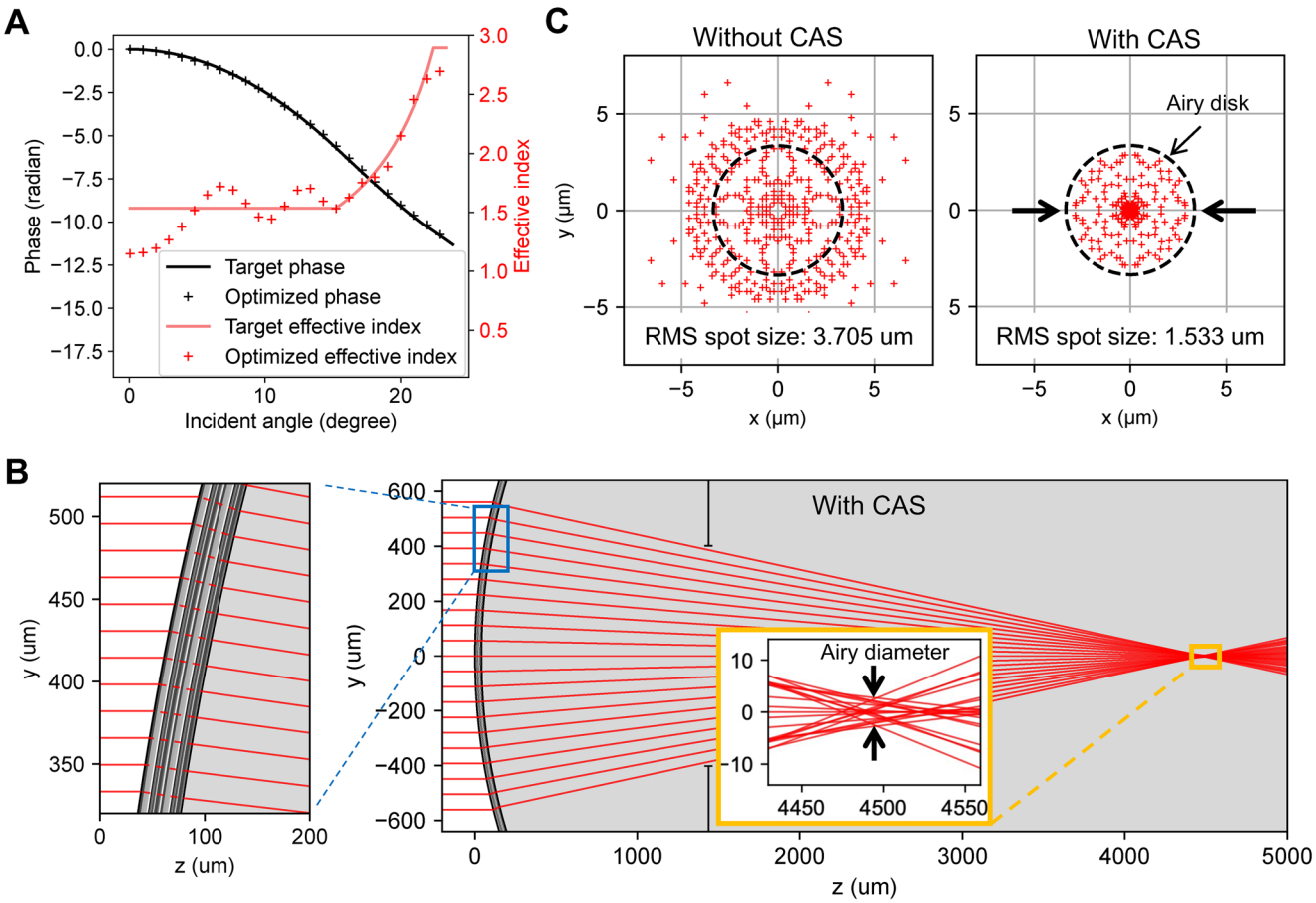


**FIGURE 3** | Aberration correction capabilities of a physical CAS-refractive system. (A) Target (solid lines) and optimized (crosses) angular-dependent effective index (red) and phase (black) profiles of a 40 μm-thick CAS. The optical system parameters are consistent with those in Figure 2D. The upper and lower bounds of the effective index values are set to the refractive indices of silicon and silica to facilitate feasible physical CAS implementation. (B) Ray diagram showing beam propagation through an air-glass CAS-refractive interface, calculated using a hybrid ray tracing-TMM approach. Left inset: magnified view of refraction at the CAS interface. Right inset: magnified view of the rays near the focal plane. (C) Spot diagrams of the focal spot from a system without (left) and with (right) the CAS. The root mean square (RMS) spot size and Airy disk diameter reference are presented for both cases.

greater than one, in a manner that is consistent with the curves in Figure 2D. These regimes correspond to CAS performing space compression and space expansion, respectively.

## 2.2 | Aberration Correction in Air-to-Glass Systems

Using our method for calculating CAS effective indices, we can design and model a physical CAS-refractive system. The refractive surface and aperture parameters are the same as above, and the CAS thickness is set to 40 μm and comprises a 36-layer freeform thin-film stack. The thin films take continuous refractive index values with the upper bound set by silicon. CAS made of binary stacks of silicon and silica can also be designed using the same methods, at a slight expense in performance. We assume a focal plane offset of +21 μm, which sets the range of required effective indices to moderate values. We use our differentiable ray tracer to determine our CAS effective index profile, and the result is shown in Figure 3A together with its corresponding angle-dependent phase response. The upper limit in effective index is near 3, which can be readily accommodated by our silicon-silica materials system. The effective index at lower incidence angles is clipped to 1.5, which is done to improve the tractability of the thin film CAS design task. While this approximation for paraxial ray response deviates from conditions required for ideal spherical aberration correction, the impact is minimal because paraxial rays generally generate fewer aberrations than marginal rays. Optimization of the thin film CAS stack is performed using a gradient-based algorithm [22]. The angular dependent effective indices and phase responses of the designed CAS show good agreement with the targeted values (Figure 3A).

To model the physical CAS-refractive system, we use a hybrid ray tracing-TMM approach in which incident and transmitted ray propagation is captured by ray tracing, and the lateral beam shifts in the CAS are determined by the transfer function of the thin film stack calculated by TMM. Snell's law is used at the air-CAS and CAS-glass interfaces, and the change in the surface normal direction at the CAS-glass interface due to lateral beam shifting is accounted for. The ray and spot diagrams in Figure 3B,C, respectively, demonstrate that the CAS-refractive system displays significant aberration reduction and diffraction-limited performance. The root-mean-squared (RMS) spot size of

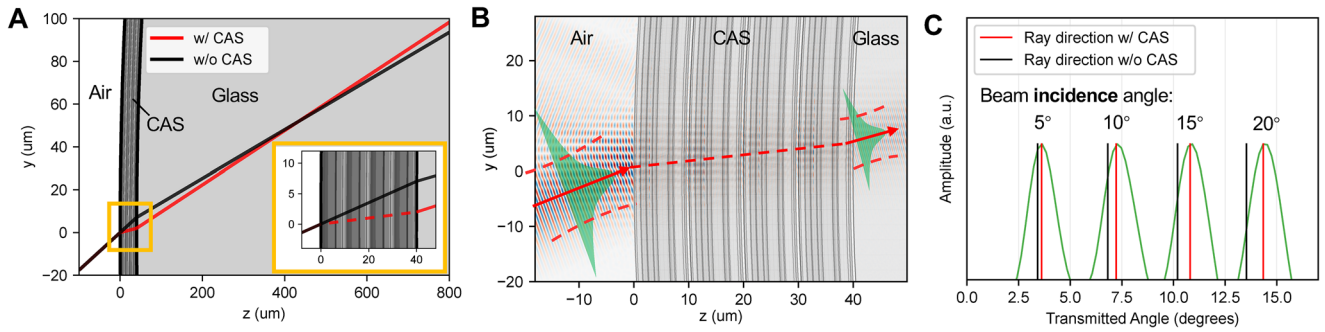


**FIGURE 4** | Comparison of ray tracing-TMM model and full-wave analysis for CAS. (A) Ray tracing diagram of an optimized CAS-refractive system performed using our hybrid ray tracing-TMM approach (red), together with a ray tracing reference of the system without CAS (black). The transmitted beam from the CAS experiences a clear lateral shift and modified tilt angle at the interface. Inset: magnified view of the CAS showing the multilayer structure. (B) Full-wave simulation of a Gaussian beam incident on the same CAS in (A), where CAS curvature has been taken into account. The transmitted Gaussian beam displays a shift and modification in tilt angle that is consistent with that calculated by our ray tracing-TMM approach. (C) Plots of angular power spectra of the transmitted Gaussian beams from (B) (green curves), calculated for incident beam angles of 5°, 10°, 15°, and 20°, together with the transmitted ray angle calculated using our ray tracing-TMM approach (red). The transmitted ray angle for a system without the CAS (black) is also shown.

this system is 1.53 μm and is within the boundaries of the Airy disk. In contrast, without the CAS, the refractive surface displays an RMS spot size of 3.71 μm.

Ray displacement within the CAS and the modified tilt of the transmitted ray collectively contribute to the aberration correction. To provide a quantitative example, we analyze the marginal ray from the system in Figure 3, which has an incident angle of 22.9°. At this angle, the effective index of the 40-μm-thick CAS is 2.70, resulting in a refractive angle of 8.3° within the CAS that imparts a lateral displacement of 5.8 μm along the CAS tangential direction. The ray then exits the CAS-glass interface with a final tilt angle of 7.3° relative to the z-axis. For comparison, the marginal ray in a system without a CAS would exit at a 7.7° angle. This angular change is a combined result of both the new refraction angle and the 5.8 μm lateral shift, which moves the ray to a point on the curved surface with a different normal. Given the long focal length of the spherical surface (≈ 4.4 mm), this small angular correction is amplified, resulting in a large vertical shift of 35 μm at the focal plane. This final displacement is the major driver of both the focal plane offset effect and the aberration correction. The fact that a small change in the ray's tilt angle can have such a large impact on the focal plane motivates the need for a rigorous full-wave validation of our model's predictions, which we perform in the following section.

## 2.3 | Model Validation with Full-Wave Analysis

One of the key assumptions that we have used throughout this discussion is that the CAS thickness is sufficiently small compared to the radius of curvature of the refractive surface. In this limit, we describe the CAS surface as locally flat, model the thin films locally using TMM, and use Snell's law at the air-CAS and CAS-glass interfaces. Technically, the formalisms behind the TMM method and Snell's law are based on purely planar systems, making their application to our slightly curved CAS an approximation. To explore the validity of this approximation, we compare our hybrid ray tracing-TMM simulator with a full-wave analysis of a curvilinear CAS. We test our approach in a more extreme curvature regime compared to the example in Figure 3 and consider a refractive with a radius of curvature of only 400 μm with a conformal 40 μm-thick CAS. More details of the problem setup and results are in the Supporting Information Section.

A hybrid ray tracing-TMM analysis of an optimized CAS on the curved refractive surface with a 400 μm radius of curvature is shown in Figure 4A, together with rays interacting with just the curved refractive surface as a benchmark. The CAS is specified to have a large effective refractive index for the given incidence angle, and it produces a visible downward lateral shift of the transmitted ray. An examination of the transmitted rays with and without the CAS makes clear that the CAS not only laterally displaces the incident ray, but it also noticeably alters the transmitted ray direction. This change in transmitted ray direction ultimately dictates the focusing properties of the ray.

Full-wave finite element simulations of the same CAS-refractive system, which account for the detailed wave physics and finite curvature of the system, show good agreement with our hybrid ray tracing-TMM approach. The full-wave simulation of the same setup from Figure 4A is presented in Figure 4B, where the incident ray is modeled as a Gaussian beam with an 8 μm beam waist radius. Wave propagation through the CAS itself is characterized by extensive reflection and transmission interactions at the thin film interfaces, which signifies highly non-local behavior within this volumetric photonic system. The transmitted beam has the form of a Gaussian with a reduced beam waist due to its transmission in glass. The position and direction of the transmitted beam are readily quantified, and it matches well with parameters calculated from Figure 4A. A more comprehensive assessment of the CAS-refractive system for different incidence angles is shown in Figure 4C for incidence angles spanning 5° to 20°. Here, the angular power spectra of the transmitted beams are plotted for the full-wave simulations, together with the exit ray direction calculated using our ray tracing-TMM approach, and they show good agreement. These simulations also demonstrate clear differences in transmitted ray

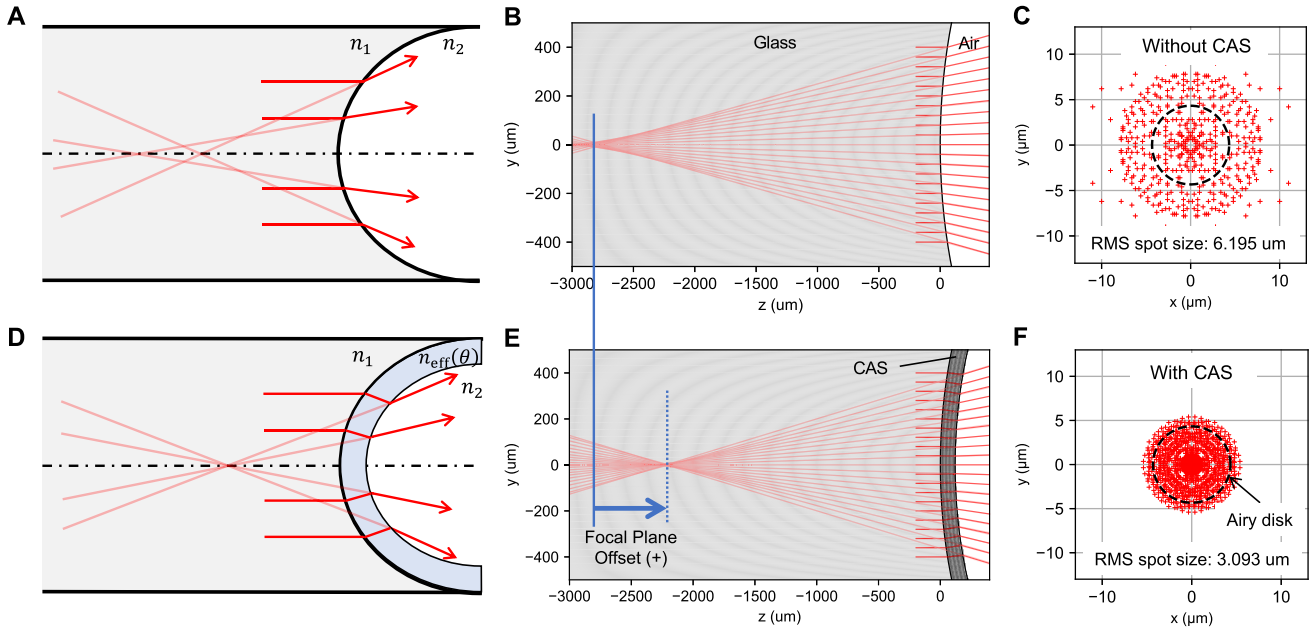


**FIGURE 5** | Aberration correction in a spherical glass-to-air CAS-refractive system. (A,D) Aberrations in a (A) conventional spherical refractive system and (D) CAS-refractive system. The conventional system contains spherical aberration that manifests in the virtual image focal plane, while the CAS-refractive can explicitly correct for spherical aberration. Deep red lines indicate actual rays while light red lines indicate virtual rays. (B,E) Ray diagrams for the system (B) without and (E) with the CAS. The CAS-refractive as designed displays a positive focal plane offset of 800 μm, demonstrating that the CAS can enhance the optical power of the system. (C,F) Spot diagrams for the system (C) without and (F) with the CAS. The addition of the CAS reduces the spot size by half and enables nearly diffraction-limited performance.

angle between the optical system with and without the CAS, signifying the importance of accounting for and tailoring the exit beam angle when designing CAS-based systems.

### 2.4 | Aberration Correction in Glass-to-Air Systems

Following our discussion of CAS for air-to-glass systems, we perform an analysis of CAS for glass-to-air convex spherical surfaces. The physical properties of this system (i.e., glass refractive index, interface radius of curvature, and wavelength) are consistent with those in Figure 3. The f-number of the system is 3.55. Similar to the case of air-to-glass spherical surfaces, glass-to-air interfaces without CAS have spherical symmetry, which introduces spherical aberrations. These aberrations are easily visualized when considering incident parallel rays: the formed virtual image within the glass shows marginal rays focusing closer to the interface compared to the paraxial rays (Figure 5A). Ray tracing is performed to quantify the impact of these aberrations on system performance, and ray (Figure 5B) and spot (Figure 5C) diagrams for the on-axis field show that the focal spot has a root mean square spot size that is more than twice as large as the Airy disk size.

We show that CAS can correct for spherical aberrations for a specified focal plane offset (Figure 5D). We consider the case of a positive 800 μm focal plane offset relative to the paraxial focal plane, which requires the CAS to have relatively large effective indices for small ray angles in order to shift the paraxial rays in this manner. We use our differentiable ray tracer to solve for the CAS angle-dependent effective index profile and TMM-based optimization to design a 120 μm-thick, 120-layer CAS with the corresponding transfer function. More details of the design are in the Supporting Information Section. The results of a hybrid ray tracing-TMM simulation and corresponding spot diagram at the new focal plane are shown in Figure 5E,F. The ray diagram shows that the CAS-refractive system displays the large desired focal plane shift, indicating the ability for CAS to modify the power of the spherical interface in a manner that can lead to overall system compression. The focal spot size is reduced by a factor of two compared to that from the refractive system without a CAS and is nearly diffraction-limited.

## 3 | Conclusion

In summary, we present CAS as a new nanophotonic device for optical design and show that hybrid CAS-refractive systems can combine the unique non-local wave-based physics of CAS with the ray-based physics of refractives to enable new aberration correction capabilities in rotationally symmetric optical systems. Compared to conventional aberration correction concepts, which utilize aspherical surfaces or local phase responses with *spatial* dependence, CAS enables customized angle-dependent optical responses at all spatial positions, providing a qualitatively different approach to optical response engineering over a wide range of field angles. We show that a CAS-refractive spherical surface can explicitly correct for all aberrations except for Petzval curvature. We additionally show that CAS can simultaneously modify and enhance the focusing power of an optical system, leading to a reduction in system size exceeding that of equivalent planar spaceplate systems.

There are many new research directions that can build on these concepts. CAS can be extended to support customized multi-wavelength or broadband responses, which can be used to realize broadband hybrid optical systems and be dispersion-engineered to enable chromatic aberration correction responses and multi-functional wavelength-multiplexed capabilities [22]. CAS can also be adapted to other types of refractive surfaces, including aspheric and freeform surfaces, and multiple CAS can be utilized in multi-element optical systems to further enhance capabilities and performance. Ultimately, new concepts in optical design and aberration theory will need to be developed to rigorously understand how to properly and systematically design optical systems with CAS. While spaceplates have been experimentally demonstrated using thin film stacks [43], we envision that more general approaches to CAS, utilizing stacks of subwavelength-scale periodic structured media, can enable even more diverse non-local optical responses.


### Acknowledgements

This work was supported by the National Aeronautics and Space Administration under Award No. 80NSSC21K0220 and the Office of Naval Research under Award No. N00014-20-1-2105. R. Lupoiu acknowledges support from the Knight-Hennessy Fellowship. The authors thank E. Wollack of NASA for helpful discussions and feedback.


### Conflicts of Interest

The authors declare no conflicts of interest.

### Data Availability Statement

The data that support the findings of this study are available in the supplementary material of this article.

### References


1. R. E. Fischer, B. Tadic-Galeb, P. R. Yoder, et al., *Optical System Design* (Citeseer, 2000), 599.

2. N. Yu, P. Genevet, M. A. Kats, et al., "Light Propagation With Phase Discontinuities: Generalized Laws of Reflection and Refraction," *Science* 334, no. 6054 (2011): 333–337.

3. N. Yu and F. Capasso, "Flat Optics With Designer Metasurfaces," *Nature Materials* 13, no. 2 (2014): 139–150.

4. A. Arbabi, Y. Horie, A. J. Ball, M. Bagheri, and A. Faraon, "Subwavelength-Thick Lenses With High Numerical Apertures and Large Efficiency Based on High-Contrast Transmitarrays," *Nature Communications* 6, no. 1 (2015): 7069.

5. M. Khorasaninejad, W. T. Chen, R. C. Devlin, J. Oh, A. Y. Zhu, and F. Capasso, "Metalenses at Visible Wavelengths: Diffraction-Limited Focusing and Subwavelength Resolution Imaging," *Science* 352, no. 6290 (2016): 1190–1194.

6. A. Arbabi, E. Arbabi, S. M. Kamali, Y. Horie, S. Han, and A. Faraon, "Miniature Optical Planar Camera Based on a Wide-Angle Metasurface Doublet Corrected for Monochromatic Aberrations," *Nature Communications* 7, no. 1 (2016): 13682.

7. B. Groever, W. T. Chen, and F. Capasso, "Meta-Lens Doublet in the Visible Region," *Nano Letters* 17, no. 8 (2017): 4902–4907.

8. T. Phan, D. Sell, E. W. Wang, et al., "High-Efficiency, Large-Area, Topology-Optimized Metasurfaces," *Light: Science & Applications* 8, no. 1 (2019): 48.

9. M. Pan, Y. Fu, M. Zheng, et al., "Dielectric Metalens for Miniaturized Imaging Systems: Progress and Challenges," *Light: Science & Applications* 11, no. 1 (2022): 195.

10. X. Hua, Y. Wang, S. Wang, et al., "Ultra-Compact Snapshot Spectral Light-Field Imaging," *Nature Communications* 13, no. 1 (2022): 2732.

11. Z. Shen, F. Zhao, C. Jin, S. Wang, L. Cao, and Y. Yang, "Monocular Metasurface Camera for Passive Single-Shot 4D Imaging," *Nature Communications* 14, no. 1 (2023): 1035.

12. S. Shrestha, A. Overvig, M. Lu, A. Stein, and N. Yu, "Multi-Element Metasurface System for Imaging in the Near-Infrared," *Applied Physics Letters* 122, no. 20 (2023): 201701.

13. T. Dai, T. Phan, E. W. Wang, et al., "Snapshot Mueller Spectropolarimeter Imager," *Microsystems & Nanoengineering* 9, no. 1 (Oct 2023): 125.

14. Y. Zhou, Y. Shao, C. Mao, and J. A. Fan, "Inverse-Designed Metasurfaces With Facile Fabrication Parameters," *Journal of Optics* 26, no. 5 (2024): 055101.

15. R. Lupoiu, Y. Shao, T. Dai, C. Mao, K. Edée, and J. A. Fan, "A Multi-Agentic Framework for Real-Time, Autonomous Freeform Metasurface Design," *Science Advances* 11, no. 44 (2025): eadx8006.

16. A. Overvig, S. A. Mann, and A. Alù, "Spatio-Temporal Coupled Mode Theory for Nonlocal Metasurfaces," *Light: Science & Applications* 13, no. 1 (2024): 28.

17. A. Overvig and F. Monticone, "Nonlocal Metasurfaces: Universal Modal Maps Governed by a Nonlocal Generalized Snell's Law," *Nanophotonics* 14, no. 23 (2025): 3851–3860.

18. Y. Chen, R. Fleury, P. Seppecher, G. Hu, and M. Wegener, "Nonlocal Metamaterials and Metasurfaces," *Nature Reviews Physics* 7 (2025): 1–14.

19. E. M. Arup, L. Liu, H. Mekonnen, D. Bosomtwi, and V. E. Babicheva, "Metasurfaces With Multipolar Resonances and Enhanced Light–Matter Interaction," *Nanomaterials* 15, no. 7 (2025): 477.

20. F. Monticone, N. A. Mortensen, A. I. Fernández-Domínguez, et al., "Roadmap on Nonlocality in Photonic Materials and Metamaterials," *arXiv preprint arXiv:2503.00519* (2025).

21. Q. Liao, Y. Liu, F. Sun, et al., "High-Performance Spaceplates Through Anti-Optical Null Medium," *Optics & Laser Technology* 192 (2025): 113856.

22. Y. Shao, R. Lupoiu, J. Jiang, Y. Zhou, T. D. Milster, and J. A. Fan, "Multifunctional Spaceplates for Optical Aberration Correction," *ACS Photonics* 11, no. 4 (2024): 1753–1760.

23. P. Yeh and M. Hendry, "Optical Waves in Layered Media," (1990): 77–78.

24. H. Kwon, D. Sounas, A. Cordaro, A. Polman, and A. Alù, "Nonlocal Metasurfaces for Optical Signal Processing," *Physical Review Letters* 121, no. 17 (2018): 173004.

25. H. Cai, S. Srinivasan, D. A. Czaplewski, et al., "Inverse Design of Metasurfaces With Non-Local Interactions," *npj Computational Materials* 6, no. 1 (2020): 116.

26. Y. Zhou, H. Zheng, I. I. Kravchenko, and J. Valentine, "Flat Optics for Image Differentiation," *Nature Photonics* 14, no. 5 (2020): 316–323.

27. J.-H. Song, J. van de Groep, S. J. Kim, and M. L. Brongersma, "Non-Local Metasurfaces for Spectrally Decoupled Wavefront Manipulation and Eye Tracking," *Nature Nanotechnology* 16, no. 11 (2021): 1224–1230.

28. C. Guo, M. Xiao, M. Orenstein, and S. Fan, "Structured 3D Linear Space–Time Light Bullets by Nonlocal Nanophotonics," *Light: Science & Applications* 10, no. 1 (2021): 160.

29. O. Y. Long, C. Guo, W. Jin, and S. Fan, "Polarization-Independent Isotropic Nonlocal Metasurfaces With Wavelength-Controlled Functionality," *Physical Review Applied* 17, no. 2 (2022): 024029.

30. Y. Zhou, S. Guo, A. C. Overvig, and A. Alù, "Multiresonant Nonlocal Metasurfaces," *Nano Letters* 23, no. 14 (2023): 6768–6775.

31. Z. Jiang, T. Dai, S. Guo, et al., "Near-Field Optical Mode Engineering-Enabled Freeform Nonlocal Metasurfaces," *arXiv preprint arXiv:2506.15495* (2025).

32. T. Dai, Y. Shao, C. Mao, et al., "Shaping Freeform Nanophotonic Devices With Geometric Neural Parameterization," *npj Computational Materials* 11, no. 1 (2025): 259.

33. M. Gerken and D. A. Miller, "Multilayer Thin-Film Structures With High Spatial Dispersion," *Applied Optics* 42, no. 7 (2003): 1330–1345.

34. C. Jin and Y. Yang, "Transmissive Nonlocal Multilayer Thin Film Optical Filter for Image Differentiation," *Nanophotonics* 10, no. 13 (2021): 3519–3525.

35. C. Guo, H. Wang, and S. Fan, "Squeeze Free Space With Nonlocal Flat Optics," *Optica* 7, no. 9 (2020): 1133–1138.

36. O. Reshef, M. P. DelMastro, K. K. Bearne, et al., "An Optic to Replace Space and Its Application Towards Ultra-Thin Imaging Systems," *Nature Communications* 12, no. 1 (2021): 3512.

37. A. Chen and F. Monticone, "Dielectric Nonlocal Metasurfaces for Fully Solid-State Ultrathin Optical Systems," *ACS Photonics* 8, no. 5 (2021): 1439–1447.

38. M. Mrnka, E. Hendry, J. Láčík, et al., "Space Squeezing Optics: Performance Limits and Implementation at Microwave Frequencies," *APL Photonics* 7, no. 7 (2022): 076105.

39. J. T. Pagé, O. Reshef, R. W. Boyd, and J. S. Lundeen, "Designing High-Performance Propagation-Compressing Spaceplates Using Thin-Film Multilayer Stacks," *Optics Express* 30, no. 2 (2022): 2197–2205.

40. M. Pahlevaninezhad and F. Monticone, "Multi-Color Spaceplates in the Visible," *ACS Nano* 18, no. 42 (2024): 28585–28595.

41. F. J. Díaz-Fernández, L. M. Má nez-Espina, A. Díaz-Rubio, and V. Asadchy, "Broadband Transparent Huygens' Spaceplates," *npj Nanophotonics* 1, no. 1 (2024): 30.

42. M. Mrnka, T. Whittaker, D. B. Phillips, E. Hendry, and W. Whittow, "Shrinking a Gradient-Index-Lens Antenna System With a Spaceplate," *Physical Review Applied* 22, no. 3 (2024): 034039.

43. R. Hogan, Y. Mamchur, R. M. Cordova-Castro, et al., "Experimental Demonstration of High Compression of Space by Optical Spaceplates," *arXiv preprint arXiv:2506.20647* (2025).

44. I. V. Shadrivov, A. A. Zharov, and Y. S. Kivshar, "Giant Goos–Hänchen Effect at the Reflection From Left-Handed Metamaterials," *Applied Physics Letters* 83, no. 13 (2003): 2713–2715.

45. S. Du, W. Zhang, W. Liu, Y. Zhang, M. Zhao, and L. Shi, "Realization of Large Transmitted Optical Goos–Hänchen Shifts in Photonic Crystal Slabs," *Nanophotonics* 11, no. 20 (2022): 4531–4536.

46. D. A. Miller, "Why Optics Needs Thickness," *Science* 379, no. 6627 (2023): 41–45.

47. P. M. Martin, Ed., *Handbook of Deposition Technologies for Films and Coatings: Science, Applications and Technology*, 3rd ed William Andrew (2010).

48. A. Luce, A. Mahdavi, F. Marquardt, and H. Wankerl, "Tmm-Fast, a Transfer Matrix Computation Package for Multilayer Thin-Film Optimization: Tutorial," *Journal of the Optical Society of America A* 39, no. 6 (2022): 1007–1013.

49. K. Shastri, O. Reshef, R. W. Boyd, J. S. Lundeen, and F. Monticone, "To What Extent Can Space Be Compressed? Bandwidth Limits of Spaceplates," *Optica* 9, no. 7 (2022): 738–745.

## Supporting Information

Additional supporting information can be found online in the Supporting Information section.

**Supporting File 1:** lpor70818-sup-0001-SuppMat.pdf.

**Supporting File 2:** lpor70818-sup-0002-DataFile.xlsx.